Post-Print

J. Fu, L. Vigevano
Aeroacoustic Modeling of Helicopter Transonic Rotor Noise
Aerospace Science and Technology, Vol. 122, 2022, 107430 (15 pages)
doi:10.1016/j.ast.2022.107430

Aeroacoustic modelling of helicopter transonic rotor noise

Jinbin Fu[a,*], Luigi Vigevano[a]

[a]*Department of Aerospace Science and Technology, Politecnico di Milano, Via La Masa, 34, Milano, 20156, Italy*

Abstract

The noise propagation of an helicopter rotor with blade tip in transonic regime is numerically simulated. To calculate the acoustic characteristics of the helicopter rotor, a novel CFD/Penetrable Surface Ffowcs Williams-Hawkings (PS-FWH) hybrid approach is established. The approach is characterized by the solution of the Reynolds-Averaged Navier-Stokes (RANS) equations on a Chimera system of overset meshes, coupled with an in-house acoustic code (ROCAAP), which employs the PS-FWH method with a Marching-Cube Emission-Surface (MCES) integral algorithm, for the noise propagation. The hybrid approach is validated through two databases. The well-known Caradonna-Tung hovering rotor test is used to assess the pressure distribution at each cross-section along the blade. The transonic acoustic survey of the UH-1H rotor is adopted to evaluate the time domain noise signal with different blade tip Mach numbers during hover. The capabilities of the hybrid method to predict helicopter transonic rotor noise are demonstrated through the achieved good correlation with experimental data.

Keywords: Helicopter rotor; Transonic acoustic; Penetrable Surface Ffowcs Williams-Hawkings method; Marching-Cube Emission-Surface integral algorithm.

*Corresponding author at: Department of Aerospace Science and Technology, Politecnico di Milano, Milan, Italy
E-mail address: jinbin.fu@polimi.it (J. Fu)

1. Introduction

High-speed flight has always been the quest for helicopters. However, High-Speed Impulsive (HSI) noise, engendered by the shock delocalization on the advancing rotor blade, challenges a further increase of helicopter flight speed. For this reason, an efficient tool that allows predicting the helicopter rotor HSI noise is essential for supporting the design and for reducing the HSI noise level.

In the past few decades, integral methods that separate the noise source computation and noise propagation have been able to effectively predict the rotor noise. The flow domain around rotor blades is determined using a CFD solver, and an integral method is employed to depict how the acoustic signals propagate to the far-field. The Kirchhoff method [1, 2], the Impermeable Surface Ffowcs Williams-Hawkings (IS-FWH) equation [3–5], and the Penetrable Surface Ffowcs Williams-Hawkings (PS-FWH) equation [6, 7] are the three most representative approaches for noise propagation.

The IS-FWH equation is based on Lighthill's acoustic analogy [8]. It allows calculating the acoustic pressure signal at a far-field observer from the knowledge of the flow quantities on the blade surface and in the volume surrounding it. In this formulation, the noise may be interpreted as the sum of the thickness and loading source distributions over the control surface and a quadrupole nonlinear source distribution over the volume outside the control surface [9]. The IS-FWH equation is particularly suitable for predicting the subsonic rotor noise; however, when it comes to the transonic rotor noise prediction, the IS-FWH equation presents low-efficiency as the volume integration is time consuming and challenging to implement. The Kirchhoff method, which involves integration over a closed control surface around the source in the linear flow region, is more attractive in predicting transonic noise since no volume integration is required, but it is computationally demanding for the flow simulation, as the control surface must be placed sufficiently far from the source to ensure the linear wave propagation

outside the control surface [10]. Furthermore, this approach does not provide any information about the noise generation mechanism. For these reasons, P.di Francescantonio [11] derived the PS-FWH equation and employed the Formulation 1A of Farassat [9], enabling the use of the FW-H equation on a penetrable control surface not required to be in the linear flow region. The PS-FWH equation has proved to be successful in the prediction of transonic rotor noise because the nonlinear effects inside the control surface could be take into consideration. K.S. Brentner *et al.* [1] compared the PS-FWH equation with the Kirchhoff method for HSI noise prediction. A.S. Morgans *et al.* [12] focused on the effect of control surface with different sizes on transonic rotor noise prediction. Chen *et al.* [13] developed an adaptive integral surface for predicting the HSI noise.

In terms of the integral formulation, both the Retarded-Time and the Emission-Surface algorithms of the PS-FWH equation have been employed in transonic rotor noise prediction. However, the Doppler singularity in the integral kernel prevents the Retarded-Time algorithm from obtaining a reliable noise prediction. This problem may be bypassed via the adoption of the Emission-Surface algorithm, in which the Doppler term singularity no longer appears. Over the past decades, only few researches related to the Emission-Surface algorithm have been carried out, as the construction of the emission surface is a central difficulty. Only three emission surface construction methods are available in the literature: the Marching-Cube algorithm proposed by Brentner [14], the K-Algorithm developed by Ianniello [15],[16] and the novel Emission Porous Surface (EPS) algorithm of Loiodice [17].

The Marching-Cube algorithm is based on an iso-surface construction method, usually applied in computer graphics. By transforming the control surface discretization at each source time into a three-dimensional array, the emission surface modelling becomes equivalent to an iso-surface generation problem. L.Vendemini [18] described a detailed procedure of the Marching-Cube algorithm implementation. Farassat and Brentner [19] carried out the

far-field approximation and the Marching-Cube algorithm into the IS-FWH equation to calculate the supersonic quadrupole noise. Ianniello instead proposed a different algorithm, known as the K-Algorithm, to construct the emission surface. Through a particular classification of the retarded spanwise stations and a data-adaptive procedure, the K-Algorithm is able to achieve an accurate emission surface reconstruction. Ref [20] gives a detailed description of the K-Algorithm and proposes the Emission-Surface based PS-FWH algorithm, which combines the K-Algorithm based Emission-Surface formulation with PS-FWH equation, to predict the UH-1H rotor HSI noise. Another recent Emission-Surface construction approach, which employs bifurcation analysis and an improved Retarded-Time algorithm, is developed by Loiodice *et al.* [21] and validated in Ref [17]. To the authors' knowledge, no results for a Marching-Cube Emission-Surface (MCES) based PS-FWH method has ever been published.

Despite the PS-FWH equation being widely used in predicting aerodynamically generated rotor noise, the investigation of the permeable control surface extraction from the CFD grid system is still meaningful. In particular, how to extract the porous control surface from a Chimera, multi-block, structured grid remains neglected.

This study looks to introduce a novel CFD/PS-FWH hybrid method that combines an overset, multi-block, structured grid CFD solver (ROSITA) with a PS-FWH/MCES acoustic code (ROCAAP) to model the transonic rotor noise. The main contribution of this work is twofold: to establish a strategy that could automatically extract the permeable control surface from the Chimera, multi-block, structured grid system with minimal choices from the user; to develop an Emission-Surface based PS-FWH method, which combines the MCES formulation with PS-FWH equation, for transonic rotor noise prediction.

This paper is organized as follows. Section 2 presents the numerical implementations of CFD and aeroacoustic solvers, the Marching-Cube algorithm

to construct the retarded domain, and a strategy to connect CFD and aeroacoustic method. The simulation results with respect to the validation and verification work and singularity analysis are shown in section 3. Secton 4 describes the correlation between calculated and experimental noise signals for a transonic hovering rotor. Finally, the main conclusions are summarized in section 5.

The numerical simulations in this work were mainly performed in the frame of the project ISCRA named IscrC_NOGENROT on the Galileo cluster at CINECA, made up of 1022 bi-processor 18-core Intel ®Xeon ®CPU E5-2697 v4 2.3GHz nodes interconnected by an Intel OmniPath (100Gb/s) high-performance network.

2. Numerical method

2.1. Computational fluid dynamics method (ROSITA sovler)

A parallelized multi-block, structured grid, Reynolds-Averaged Navier-Stokes (RANS) code ROSITA (Rotorcraft Software ITAly) [22] is used for analyzing the flow around rotating blades with the one-equation Spalart-Allmaras turbulence model and Chimera technique. The finite-volume formulation for Navier-Stokes equations could be written as:

$$\frac{\partial}{\partial t}\oint_{V_{ijk}} \mathbf{W} dV + \int_{S_{ijk}} (\mathbf{F_c}\cdot\mathbf{n} - \mathbf{v}\cdot\mathbf{n}\mathbf{W}) dS - \int_{S_{ijk}} \mathbf{F_d}\cdot\mathbf{n} dS = \oint_{V_{ijk}} \mathbf{S} dV \quad (1)$$

with $\mathbf{W} = [\rho, \rho u, \rho v, \rho w, \rho e^t]^T$ donates the vector of conservative variables inside the flow domain, $\mathbf{n}$ is the outward normal unit vector, $\mathbf{v}$ is the entrainment velocity vector. The expressions, $\mathbf{F_c}$ and $\mathbf{F_d}$, represent the convective flux tensor and diffusive flux tensor, respectively. V is the cell volume and S is the cell surface, $\mathbf{S}$ stands for the source term due to the movement of the relative reference frame.

In ROSITA, the space discretization leads to a system of ordinary differential equations for the rate of change of the conservative flow variables

associated with the centers of the cell volumes, the equation (1) then reads:

$$\frac{d}{dt}(V\mathbf{W})_{ijk} + \mathbf{R}_{ijk} = 0 \tag{2}$$

where $\mathbf{R}_{ijk}$ stands for the flux balance across surface S_{ijk} of the hexahedral cell (i, j, k). The flux balance can be written as:

$$\mathbf{R}_{ijk} = (\mathbf{Q_c})_{ijk} - (\mathbf{Q_d})_{ijk} - \mathbf{S}_{ijk} \tag{3}$$

where $(\mathbf{Q_c})_{ijk}$ is the convective flux balance (convective and pressure effects), $(\mathbf{Q_d})_{ijk}$ is the diffusive flux balance (viscous effects), $\mathbf{S}_{ijk}$ is the source terms. The convective flux is approximated by the use of Roe-MUSCL 2nd-order discretization, and a standard second-order central discretization calculates the diffusive flux; the components of stress tensor are discretized by the application of the Gauss theorem.

An implicit dual-time method is used for the time derivative; the equation (2) can be replaced by an implicit 2nd-order backward differential formula:

$$\frac{3(V\mathbf{W})_{ijk}^{n+1} - 4(V\mathbf{W})_{ijk}^{n} + (V\mathbf{W})_{ijk}^{n-1}}{2\Delta t} + \mathbf{R}_{ijk}^{n+1} = 0 \tag{4}$$

where the state vector $\mathbf{W}_{ijk}^{n+1}$ is solved by sub-iterations in pseudo-time at each physical time step Δt, In sub-iteration step, a generalized conjugate gradient (GCG), in conjunction with a block incomplete lower-upper preconditioner, is implemented.

2.2. Emission-Surface based PS-FWH method (ROCAAP code)

All acoustic calculations in this work were performed using the acoustic code ROCAAP (ROtorcraft Code for AeroAcoustic Prediction), a newly developed FORTRAN 90/95 code for helicopter aeroacoustic problems and is capable of running parallel on clusters. ROCAAP solves the PS-FWH equation in integral form using the MCES algorithm. The FW-H equation for a

penetrable control surface is given by:

$$\begin{aligned}\overline{\Box}^2 p' = & \frac{\partial}{\partial t}\{[\rho_0 v_n + \rho(u_n - v_n)]\delta(f)\} \\ & - \frac{\partial}{\partial x_i}\{[P'_{ij} n_j + \rho u_i(u_n - v_n)]\delta(f)\} \\ & + \frac{\overline{\partial}^2}{\partial x_i \partial x_j}[T_{ij} H(f)]\end{aligned} \tag{5}$$

where the generalized wave operator is represented by $\overline{\Box}^2 = (1/c_0^2)(\overline{\partial}^2/\partial t^2) - \overline{\nabla}^2$; $p^{'} = p - p_0$ is the acoustic pressure; ρ_0 is the density of the undisturbed medium; u_i and v_i donate the fluid and surface velocity components, respectively; n_j is the unit normal outwards to the control surface; $\delta(f)$ is the Dirac delta function; $H(f)$ is the Heaviside function; the Lighthill's equivalent stress tensor can be expressed as, $T_{ij} = \rho u_i u_j + P_{ij} - c^2(\rho - \rho_0)$; P_{ij} represents the compressive stress tensor. The three terms on the right-hand side stand for monopole thickness, dipole loading, and quadrupole contributions, respectively.

Through the use of the free-space Green's function ($\delta(t - \tau - r/c_0)/4\pi r$ with $r = |\mathbf{x} - \mathbf{y}|$) with the generalized inhomogeneous wave equation (5), a general form of the Emission-Surface based PS-FWH method can be expressed as [9]:

$$4\pi\Phi(\mathbf{x}, t) = \int_{F=0} \left[\frac{Q(\mathbf{y}, \tau)}{r\Lambda}\right]_{ret} d\Sigma \tag{6}$$

where a generic variable is expressed by $\Phi(\mathbf{x}, t)$ and the source is represented by $Q(\mathbf{y}, \tau)$; the observer and source space-time variable are denoted respectively by $(\mathbf{x}, t)$ and $(\mathbf{y}, \tau)$; r is the distance between observer and source; the Doppler term is $\Lambda = \sqrt{1 - 2M_n cos\theta + M_n^2}$, $M_n = \mathbf{M}\cdot\mathbf{n}$ and $\theta = arccos(\mathbf{n}\cdot\mathbf{r})$; Σ stands for the emission surface, a collection of points in space-time that emit signals reach the observer at the same observer time.

Hence, the Emission-Surface integral formulation of the PS-FWH equa-

tion may be derived along the line of Farassat's 1A formulation as:

$$
\begin{aligned}
4\pi p^{'}(\mathbf{x},t) = & \frac{\partial}{\partial t}\int_{\Sigma}\left[\frac{\rho_0 u_n + (\rho-\rho_0)(u_n - v_n)}{r\Lambda}\right]_{ret} d\Sigma \\
& + \frac{1}{c_0}\frac{\partial}{\partial t}\int_{\Sigma}\left[\frac{P_{nr} + \rho u_r(u_n - v_n)}{r\Lambda}\right]_{ret} d\Sigma \\
& + \int_{\Sigma}\left[\frac{P_{nr} + \rho u_r(u_n - v_n)}{r^2\Lambda}\right]_{ret} d\Sigma
\end{aligned}
\tag{7}
$$

2.3. Marching-Cube algorithm

The Marching-Cube (MC) algorithm was initially developed in computer graphics to construct high-resolution isosurfaces from scalar volume datasets. Brentner [14] first adopted this method to construct the emission surface in the IS-FWH equation. The implementation of the MC algorithm in PS-FWH equation is displayed in Figure 1 and subsequently outlined as follows:

- **Step 1:** Discretize the control surface to a set of three-dimensional cubes in the space-time domain, in which the surface is spatially parameterized in i and j direction, and the source time array is assigned to k direction.

- **Step 2:** Compute the observer time of each cube vertex via the Retarded Time equation, $t = \tau + r(\mathbf{x}, \mathbf{y}, \tau)/c_0$ and mark each vertex as 0 or 1 through the comparison with respect to the given observer time. Result in a binary format for each cube by combining these labels in sequence from v1 to v8.

- **Step 3:** Convert the binary data to the decimal for identifying the intersected edges and the number of triangles at each cube from the modified look-up tables suggested by Montari [23].

- **Step 4:** Assemble the triangles in each cube by calculating the intersections in each edge with the linearly interpolation method.

this procedure is repeated for each observer time; a set of triangles constructs the emission surface. With the MC algorithm and the Midpoint quadrature integration method [24], the equation (7) can be rewritten as:

$$4\pi p'(\mathbf{x},t) = \frac{1}{c_0}\frac{\partial}{\partial t}\sum_{i=1}^{N_{tri}}\left[\frac{Q_1(\mathbf{y}_i, t - r_i/c_0)}{r_i\Lambda_i}\right]_{ret}\Delta\Sigma_i + \sum_{i=1}^{N_{tri}}\left[\frac{Q_2(\mathbf{y}_i, t - r_i/c_0)}{r_i^2\Lambda_i}\right]_{ret}\Delta\Sigma_i \tag{8}$$

where the time derivative is calculated by a second-order finite difference over the observer time.

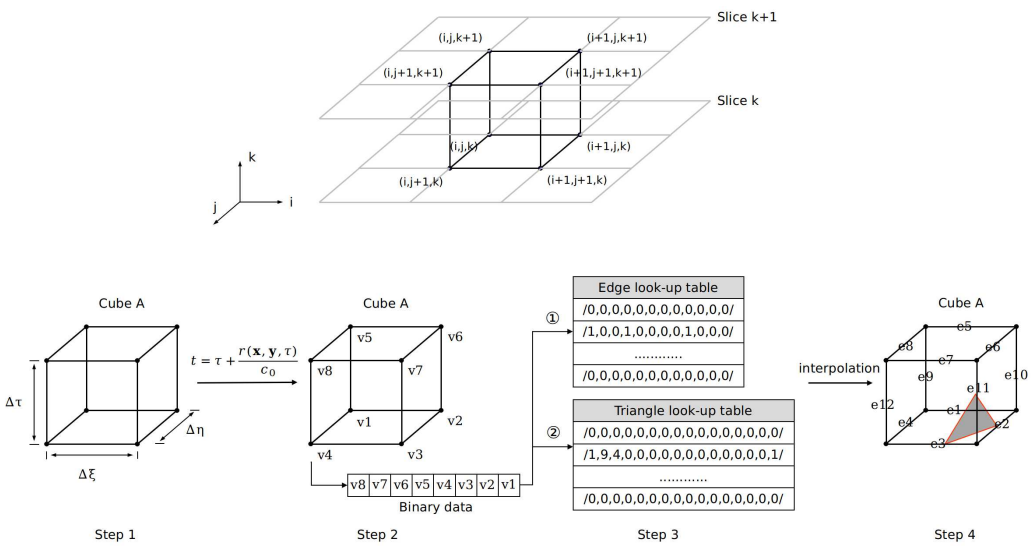

Figure 1: the steps of the MC algorithm for the emission surface construction

2.4. Connection of CFD method and PS-FWH equation

Unlike other CFD/PS-FWH hybrid methods, the grid indices in an overset, multi-block grid system are disorderly distributed within each block, so that it is difficult to specify a particular layer of the grid system as the control surface. To overcome this feature, a cylindrical permeable control surface, which should enclose most of the noise source, is automatically generated with minimal choices from the user, who needs to specify only simple geometrical parameters (radius, height, and grid dimensions). In order to

quantify the dimension of the cylindrical control surface, an ordered pair S, which evaluates how far the permeable control surface is from the blade surface, is considered as:

$$S = (|\Delta y|/c, |\Delta x|/c) \tag{9}$$

where $|\Delta y|$ represents the maximum radial extension at the blade section center, $|\Delta x|$ represents the spanwise extension outward to the blade tip section, and c is the blade section chord, as sketched in Figure 2. It is defined that the circle collapses to the airfoil surface when $|\Delta y|/c = 0.5$: in this case, the noise prediction is provided by the IS-FWH equation.

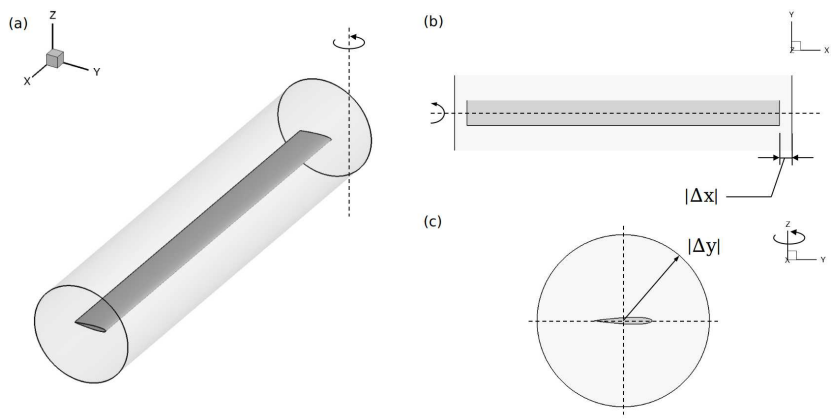

Figure 2: Control surface arrangement from different views. a) isometric view; b) top view; c) side view

An algorithm of extracting the control surface from the CFD overset, multi-block, structured grid system is presented, in which the Oct-tree search algorithm and a modified Chesshire and Henshaw algorithm [25] are used to detect the donor cells in the grid system and to interpolate the flow variables on the control surface.

The implementation of the control surface extraction algorithm within ROSITA is described by referring to a simple two-dimensional example (see Figure 3), consist of a cartesian CFD mesh (in red) and a circular control surface grid (in black).

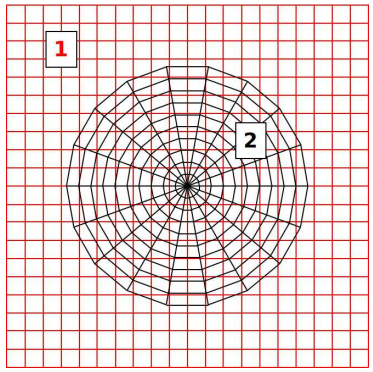

Figure 3: a simple 2D grid system with control surface

The algorithm proceeds automatically, for a given number N_s of control surfaces, via four main steps. After completion, each of the N_s control surfaces cell contains the conservative flow variables required by noise prediction. An identification array `ICHIM_CS` is used to label each of the N_c CFD grid cell centroids. The algorithm is summarized as follows::

- **Step 1: Initialization:** The first step is to initialize the identification array `ICHIM_CS`. Considering all points P of the $n-th$ CFD grid ($1 < n < N_c$), `ICHIM_CS(P,n)` is set to `0`.

- **Step 2: Find parents:** Step 2 identifies the parent grids for $s-th$ control surface grid point Q; a parent grid is a CFD grid from which point Q may be interpolated. During the Step 2 a list of valid cells is produced for subsequent use by donor finding. At the end of this step, the entries in the identification array will be:

$$\texttt{ICHIM\_CS}(\texttt{P},\texttt{n}) = \begin{cases} \texttt{0}, & \text{if point } \texttt{P} \text{ is a } \textbf{normal point} \\ -\texttt{s}, & \text{if point } \texttt{P} \text{ is a } \textbf{valid point} \text{ for the control surface } \texttt{s} \end{cases}$$

- **Step 3: Find donors:** Step 3 is finding the base donor point from the parent grids for the control surface grid interpolation. The valid points marked from the previous step are examined in sequence: for the 'target' points Q (see Figure 4), a test is made to check if a hexahedral cell

of valid donor points exists so that the solution can be interpolated. In this step, the Oct-tree fast searching algorithm is implemented to speed up the process. At the end of this step, the entries in the identification array change to:

$$\texttt{ICHIM\_CS}(\texttt{P},\texttt{n}) = \begin{cases} \texttt{0}, & \text{if point } \texttt{P} \text{ is a } \textbf{normal point} \\ -\texttt{s}, & \text{if point } \texttt{P} \text{ is a } \textbf{valid point} \\ \texttt{s}, & \text{if point } \texttt{P} \text{ is a } \textbf{base donor point} \text{ due to control surface } \texttt{s} \end{cases}$$

- **Step 4: Promote points:** Step 4 promotes the left valid points to normal points. The final entries of the identification array is :

$$\texttt{ICHIM\_CS}(\texttt{P},\texttt{n}) = \begin{cases} \texttt{0}, & \text{if point } \texttt{P} \text{ is a } \textbf{normal point} \\ \texttt{s}, & \text{if point } \texttt{P} \text{ is a } \textbf{base donor point} \text{ due to control surface } \texttt{s} \end{cases}$$

- **Step 5: Interpolation:** Step 5 is to interpolate the flow variables on the control surface with the base donor points marked from the previous steps. A trilinear interpolation is carried out to obtain the CFD data on the acoustic control surfaces for the PS-FWH equation.

Figure 5 presents a control surface extraction test for the two-bladed rotor in hover, the donor cells of the cylindrical control surfaces are shown.

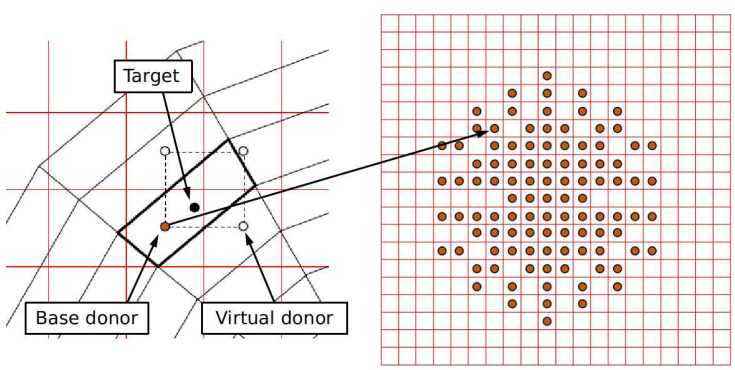

Figure 4: Search donor points

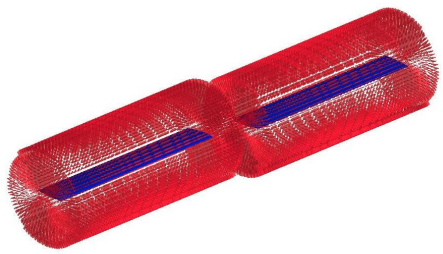

Figure 5: The extraction algorithm applied to the two-bladed rotor (donor cells in red)

3. Verification and validation studies

3.1. CFD method

The well-known Caradonna and Tung hovering rotor test case [26] is carried out as the validation case for assessing the CFD method. The two-bladed C-T rotor has rectangular, untwisted blades with an aspect ratio of 6. The blade profile is a symmetric NACA0012 airfoil. The radius of the rotor is 1.143 m and the blade chord length is 0.1905 m. The operation conditions used for validating the blade pressure distribution of the transonic test are detailed in Table.1.

A moving embedded grid system is designed for the present study, composed of background grid, and two identical body-fitted blade meshes. The grid system is reported in Figure 6. The background mesh consists of two different cylindrical grids. A coarse grid (far-field grid) is generated to represent the flow domain far from the rotor, where outer boundaries are located 4R (above), 8R (below), and 8R (radial) away from the blade hub. A finer grid (near-field grid) is created to model the flow region close to the blades. The blade grid is modelled with a C-H topology. To account for the grid discretization effect on transonic shock capturing, four structured blade grids, increasing the mesh size from 0.8 to 2.9 million cells, are generated to perform simulations. The summary of the blade grids is shown in Table. 2.

Table 1: Hover test conditions taken from the Caradonna-Tung experiment [26]

Collective pitch (°)	Rotational speed (rpm)	Tip Mach Number
8	2500	0.877

Table 2: Summary of the blade grids, employed for the Caradonna-Tung rotor simulations

Mesh	Blade elements				Volume cells (10^6)
	Upper	Lower	Span	Total	
Coarse	50	50	60	13000	0.8
Medium	120	120	60	26300	1.7
Fine	120	120	98	37586	2.4
Finer	150	150	98	45300	2.9

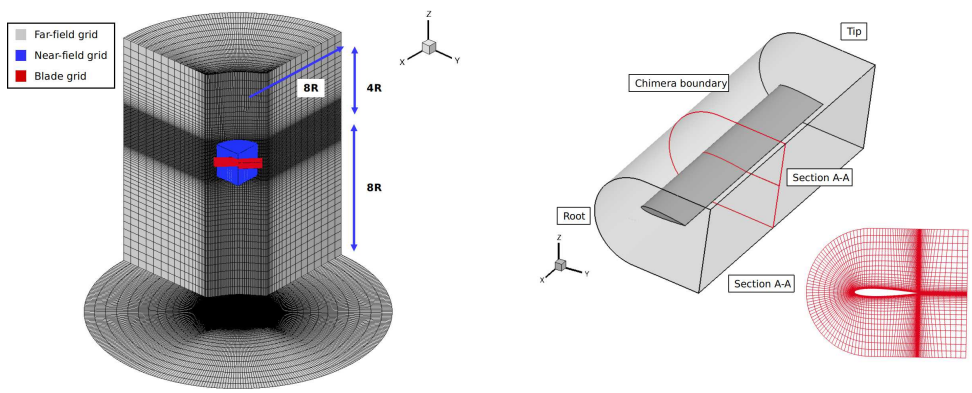

(a) Computational mesh system

(b) Caradonna-Tung rotor blade grid

Figure 6: Computational domain and detailed view of Caradonna-Tung rotor blade grid.

Figure 7 compares the calculated blade chordwise surface pressure distributions at five radial positions, r = 0.5R, 0.68R, 0.8R, 0.89R and 0.96R, with the measured data [26]. It is worth noticing that even on the coarsest grid, the CFD method is able to predict the Cp distribution with a reasonable level of precision. At r/R = 0.5 and 0.68, the sectional Cp distributions are almost identical for each grid resolution cases. At the other three sections, r/R = 0.80 - 0.96, a more smeared shock is observed for the coarsest grid case, and

it could be improved to a limited extent by adding more grid points in the direction chordwise. Overall, the CFD simulations, which give input data for rotor noise prediction, demonstrate good correlations with the experimental data.

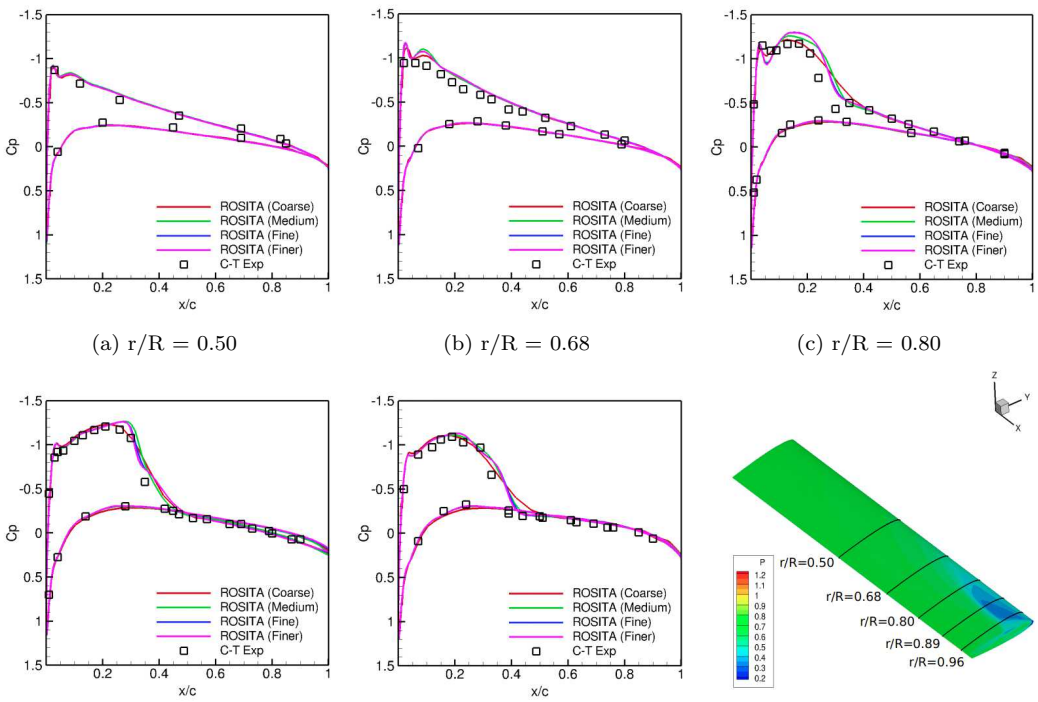

(a) r/R = 0.50 (b) r/R = 0.68 (c) r/R = 0.80

(d) r/R = 0.89 (e) r/R = 0.96 (f) Caradonna-Tung Blade

Figure 7: *Cp* comparisons on different blade cross-sections for C-T rotor in hover mode.

3.2. Emission-Surface algorithm

In the Emission-Surface algorithm, the numerical construction of the emission surface might be difficult due to the appearance of unconnected patches caused by the multiple emission times when the sources are moving supersonically. In the following subsections, a static 3D monopole source case is considered first for the verification in terms of the emission surface construction and the aeroacoustic prediction by comparing the calculated results

to analytical solutions. Secondly, the emission surface construction is tested for a blade planform rotating both in subsonic and transonic-supersonic regimes.

3.2.1. Emission surface construction of 3D stationary monopole source case

A stationary permeable spherical control surface with unit radius and a centered monopole noise source is used to test the Emission-Surface algorithm by comparing it with the analytical solution. In this study, since the MC algorithm depends on both spatial and temporal discretizations, the sphere is uniformly discretised in the spherical coordinates using variables Θ and Ψ with four different grid resolutions ($N_\Theta \times N_\Psi = 9 \times 18$, 12×24, 18×36 and 36×72); the period of noise source is discretized with NRT = 60, 120, 240 time steps. The observer is located at $\mathbf{x}_o = [5, 0, 0]$. A schematic of the test configuration is shown in Figure 8. In this case, the ratio, $\eta = S_{MC}/S_E$, is employed as an evaluation criterion to check the precision of MC reconstruction with S_{MC} marching cube emission surface area and S_E exact emission surface area. The exact area of the sphere is $S_E = 4\pi = 12.5664$.

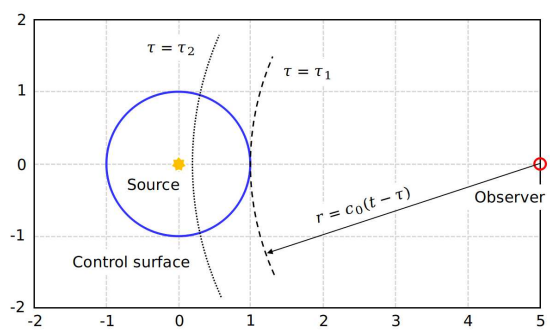

Figure 8: The test configuration for a spherical surface.

Since the spherical control surface is steady, the emission surface coincides with the permeable control surface. Figure 9 presents the emission surface corresponding to the sphere at three subsequent observer time instants in the absolute reference frame and the MC domain. The surface is rendered with the value of the emission time τ. Observing Figure 9(a), the emission

surface Σ is only a part of the sphere and then gradually grows to the entire sphere over time; see Figure 9(c) and Figure 9(e). This is because the radius of the collapse sphere, $r = c_0(t - \tau)$ (where $-\infty < \tau \leq t$), increases with the observer time. Figure 9(b), (d) and (f) correspond to the emission surface evolution in the MC domain. It can be seen that the emission surface grows from two disjoint patches to a continuous surface with observer time increases. Based on above, the calculated emission surface areas for the sphere with four different grid resolutions at three circumstances of time discretization are presented in Table 3. It is evident that the MC algorithm correctly constructs the emission surface of a stationary spherical permeable surface.

Table 3: η value of four different grid resolution spherical permeable surfaces under three temporal discretizations.

NRT	Grid resolution			
	9×18	12×24	18×36	36×72
60	0.9286	0.9579	0.9806	0.9949
120	0.9316	0.9614	0.9819	0.9952
240	0.9360	0.9640	0.9832	0.9955

3.2.2. Noise prediction of 3D stationary monopole source case

The monopole noise source is represented by a simple harmonic velocity potential function:

$$\phi(\mathbf{x}, t) = \frac{A}{4\pi r} e^{i\omega\left(t - \frac{r}{c_0}\right)} \tag{10}$$

with the velocity potential amplitude A $= 1\ m^2/s^{-1}$, angular velocity $\omega = 2\pi$ rad/s , distance of observer position and monopole source point $r = 5\ m$.

In order to measure the difference between numerical and analytical solutions to assess the implementation of the MCES algorithm, a generic parameter, ε, is defined as follows.

$$\varepsilon = \frac{\sum_{i=1}^{N_t} \sum_{j=1}^{N_x} |P_N(x_j, t_i) - P_A(x_j, t_i)|}{\sum_{i=1}^{N_t} \sum_{j=1}^{N_x} |P_A(x_j, t_i)|} \tag{11}$$

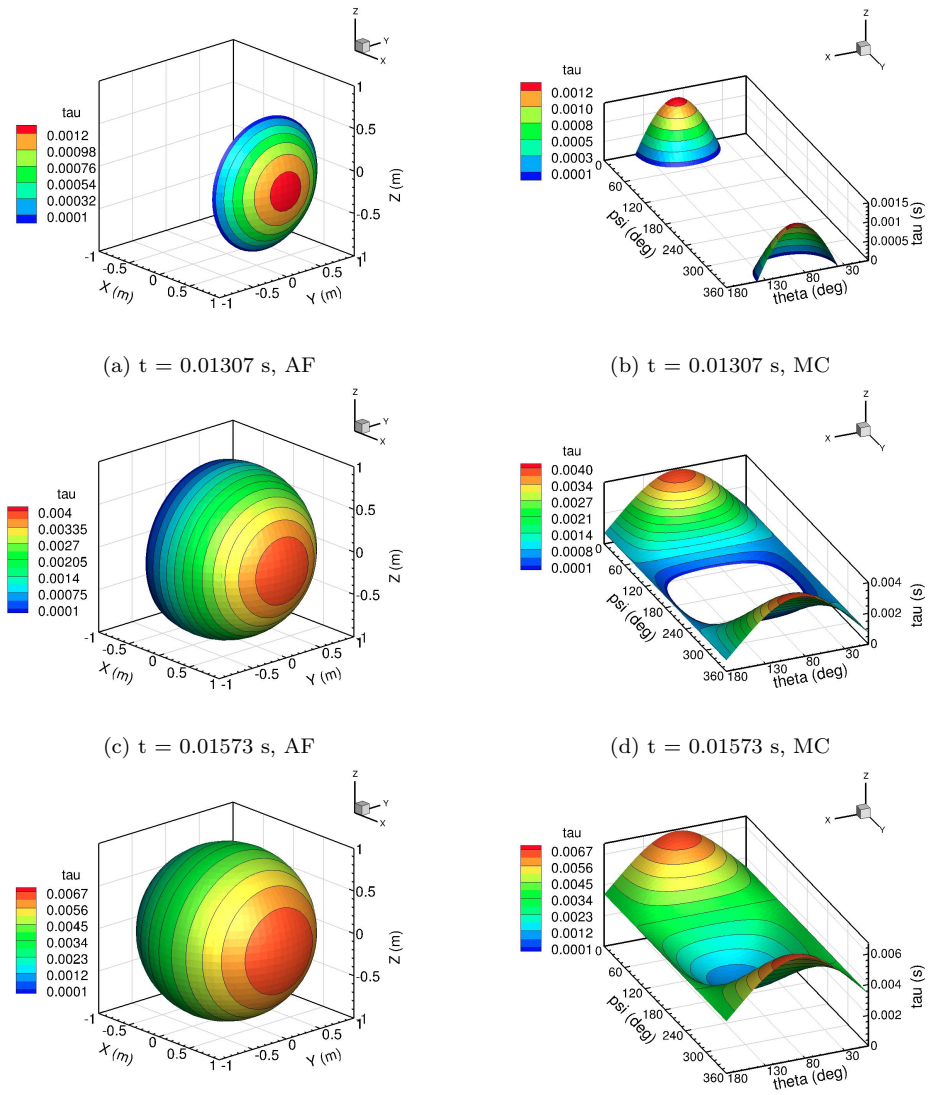

(a) t = 0.01307 s, AF

(b) t = 0.01307 s, MC

(c) t = 0.01573 s, AF

(d) t = 0.01573 s, MC

(e) t = 0.0184 s, AF

(f) t = 0.0184 s, MC

Figure 9: Σ surface of a stationary permeable spherical surface for different observer time instants in AF and MC domains.

where $P_N(x_j, t_i)$ and $P_A(x_j, t_i)$ are the computed and exact solutions at the observer position x_j and at the observer time instant t_i. N_t and N_x are the number of observer times and positions, respectively. In addition, since the

spherical control surface is uniformly discretized, the grid cell size values h corresponding to the above-defined grid space discretization are in order: h $= \pi/9, \pi/12, \pi/18, \pi/36$.

Figure 10(a) presents the acoustic results achieved with the four different grid resolution permeable control surfaces and NRT = 120, compared to the exact solution. A reasonably good agreement with minor discrepancies close to the peaks of the signal is observed. The small inaccuracy is progressively eliminated as the finer resolution grid is employed. In Figure 10(b), the numerical errors for four grid levels with three spatial discretizations are plotted on a logarithmic scale to understand the order of accuracy of the integration method. The errors are shown to drop in a second-order manner as the spatial discretization is refined, which is consistent with the accuracy of the Midpoint quadrature integration method used in the MCES algorithm. It demonstrates that the theoretical precision of the integration method is preserved.

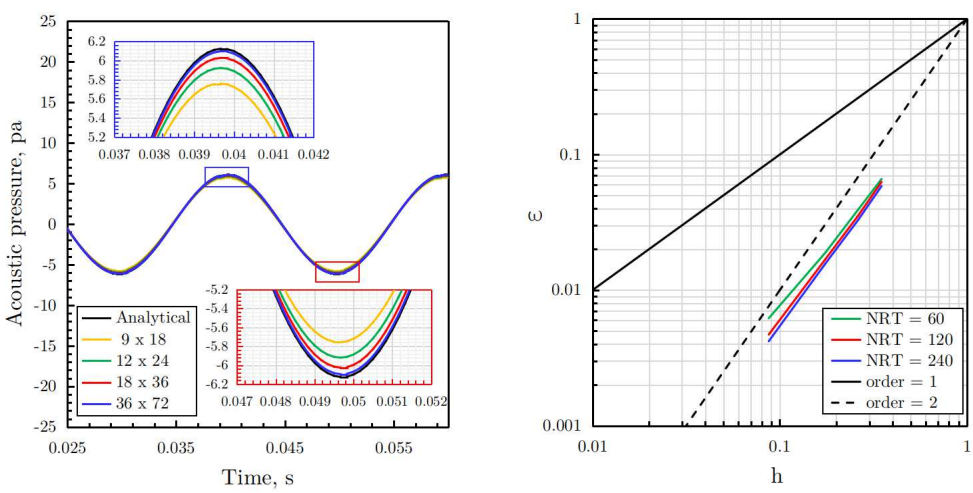

(a) (b)

Figure 10: Numerical results of the monopole source with 4 different grid resolution control surfaces, (a) Time histories of the acoustic pressure with NRT=120, (b) Numerical error in acoustic pressure for the MCES algorithm.

3.2.3. Emission surface construction of rotational blade planform

A rotational blade planform is used as a preliminary validation case for the emission surface construction. The blade planform is the 1/7-scale UH-1H rotor model with a radius of 1.045m and the aspect ratio of $AR = 13.71$. It is operated from a subsonic region, $M \approx 0.2$ at the blade root up to a supersonic regime, $M \approx 1.5$ at the blade tip. Far-field observer lies at the rotor disc plane at 3.09 rotor radii away from the rotor hub. The blade mesh is composed of upper and lower surfaces with a dimension of 10×20 (number of nodes at each section $\times$ number of sections).

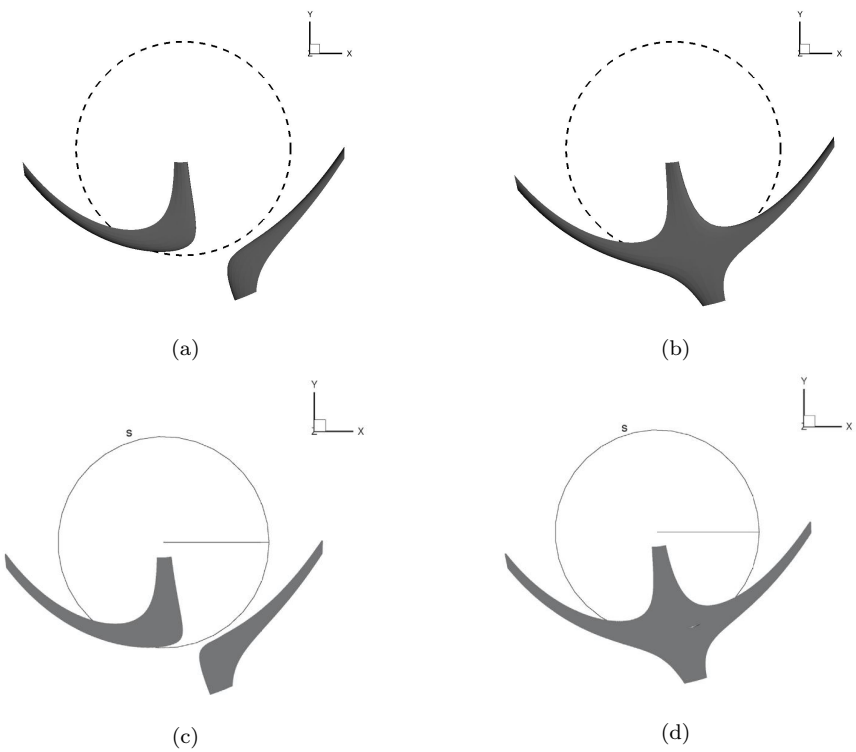

Figure 11: Emission surface of rotating blade planform at $M_{tip} = 1.5$ for two subsequent observer instants. (a), (b) results calculated by present method. (c), (d) results calculated by Loiodice [17].

The emission surface shapes at two subsequent observer time steps are illustrated in Figure 11. In Figure 11(a), emission surface consists of two

branches, which are moving towards the sonic circle of $M_r = 1$; afterwards, the two components are merged together and form a "wing-like" shape (Figure 11(b)), which is the union of all retarded position of the blade planform grid points. A qualitative comparison on the construction of the emission surface is carried out with a similar case calculated by Loiodice [17]. The emission surface prediction from Ref [17] at two similar observer time instants is presented in Figure 11(c) and (d). It is clear that emission surface prediction has the similar transformation shape as in past study [17], which means that the emission surface is constructed correctly with the use of the MC algorithm.

3.3. The Λ singularity

The singular behavior of the Λ term of equation (7) is an issue of interest for transonic noise predictions. It is recognized as the primary source for the infinite pulses in the predicted noise signals. From the mathematical point of view, $\Lambda = 0$ occurs when the control surface grid geometric and kinematic data satisfied the following conditions:

$$\begin{cases} \mathbf{M} \cdot \mathbf{n} = +1; \quad \mathbf{n} \cdot \mathbf{r} = +1 \quad \Rightarrow \Lambda = 0, \\ \mathbf{M} \cdot \mathbf{n} = -1; \quad \mathbf{n} \cdot \mathbf{r} = -1 \quad \Rightarrow \Lambda = 0 \end{cases} \tag{12}$$

which is less restrictive than the condition of Doppler singularity in Retarded-Time formulation, $\mathbf{M} \cdot \mathbf{r} = 1$.

In this section, a rotational cylindrical strip is used to clarify different behavior of the Doppler singularity between the Emission-Surface formulation and the Retarded-Time formulation. The strip is rotating along the z axis with a Mach number of $M_T = 1.1$ at the center of the strip. The cylindrical strip geometry is displayed in Figure 12(a), the rotational radius $R_T = 1.1c_0/\Omega$ ($c_0 = 340$ m/s, $\Omega = 340$ rad/s), the strip radius and width are $d_{cyl} = 0.44$ m and $w_{cyl} = d_{cyl}/5$, respectively. Figure 12(b) depicts the test configuration, in which the observer is located at $\mathbf{x}_{ob} = (5,0,0)$ m, line p1 and p2 represent the tangents to the circular trajectory passing through

the observer, t1 and t2 are the critical lines in radial direction perpendicular to lines p1 and p2. By approaching the line t2, a critical configuration of emission surface can appear due to Λ being close to zero at the leading or trailing edge of the strip (see Figure 13, the contour on the emission surface refer to the $[1/\Lambda]$ value). Whereas, no critical emission surface configuration can occur when approaching line t1, since $\mathbf{M}\cdot\mathbf{n}$ and $\mathbf{n}\cdot\mathbf{r}$ always have opposite signs.

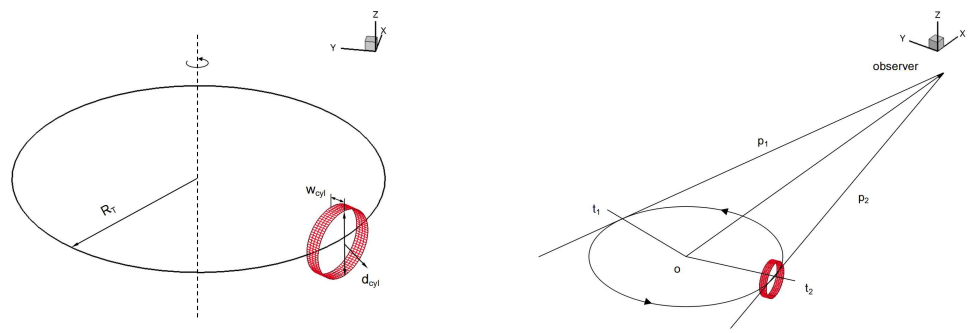

(a) (b)

Figure 12: Cylindrical strip configuration, (a) Geometry, (b) Test configuration with observer position

The time history of the $[1/\Lambda]_{max}$ term is presented in Figure 14(a) to show the Λ singularity behavior within the period of revolution. The two peak values, which are the undesirable solutions due to the absolute value of Λ being close to zero, simultaneously corresponding to the critical configurations as illustrated in Figure 13 and the conditions given in equation (12). To compare with the Doppler singularity, Figure 14(b) shows the $[1/|1-M_r|]_{max}$ time history, exhibiting multiple pulse points with the magnitude of 10^5 times of $[1/\Lambda]_{max}$, the maximum value appears at almost the same time instant of the first cusp point in Figure 14(a). The comparison of the $[1/\Lambda]_{max}$ and $[1/|1-M_r|]_{max}$ time histories indicates that the Emission-Surface algorithm is much more robust than the Retarded-Time formulation and does not need to resort to a de-singularization procedure.

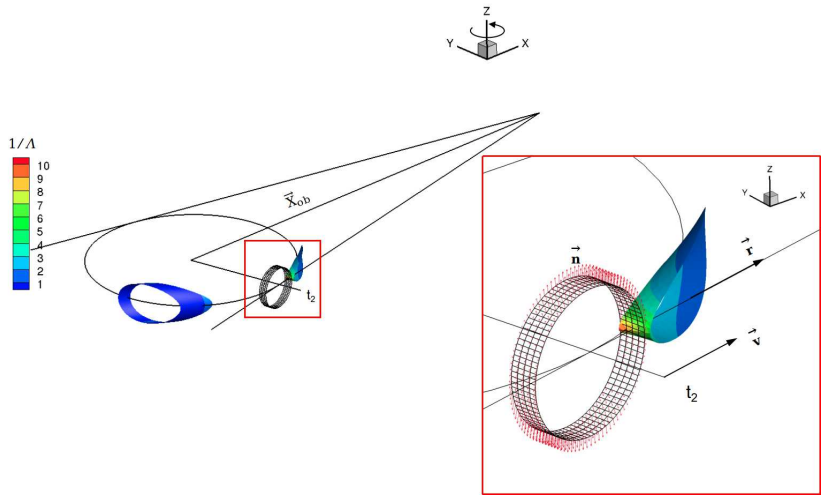

(a)

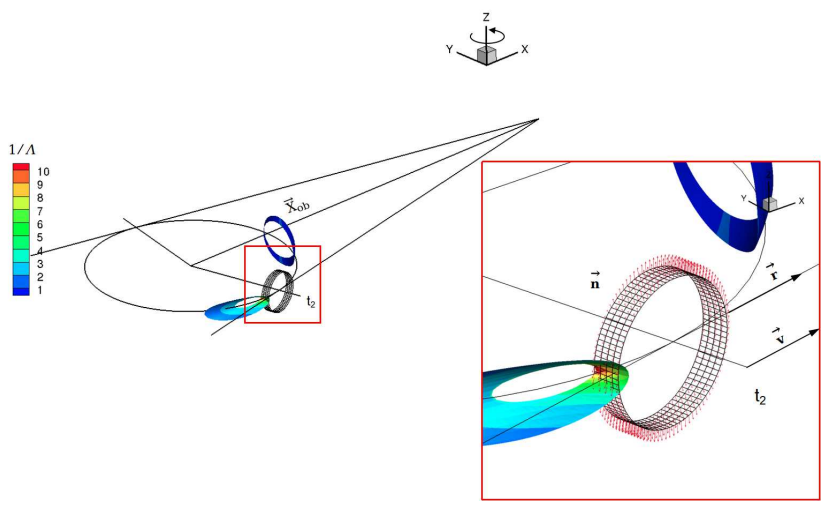

(b)

Figure 13: Two critical regions of the cylindrical strip (the emission surface colored by the $[1/\Lambda]$ value), (a) high $[1/\Lambda]$ value at the leading-edge, (b) high $[1/\Lambda]$ value at the trailing-edge

Figure 15 shows the time evolution of the computed emission surface, corresponding to the "U" shape variation of $[1/\Lambda]_{max}$ from time steps (a to (f in Figure 14(a). The first frame (Figure 15(a)) and the last frame (Figure 15(f)) depict the critical stages in which the Λ is approaching singularity. It

can be seen from Figure 15, the two emission surface branches are travelling towards each other. After few instants, the two branches come in contact (Figure 15(b)), then merge to a single large cylindrical strip (Figure 15(c)). In Figure 15(d) and Figure 15(e), the larger cylindrical strip is divided into two branches again, and the $[1/\Lambda]_{max}$ gradually reaches to the peak value (Figure 15(f)).

Loiodice [17] and Ianniello [27] also calculated a similar cylindrical strip. A quantitative comparisons of the emission surface maximum $[1/\Lambda]$ time evolution are shown in Figure 14(a). The agreement between calculated data and the results reported by Loiodice [17] and Ianniello [27] is reasonably good.

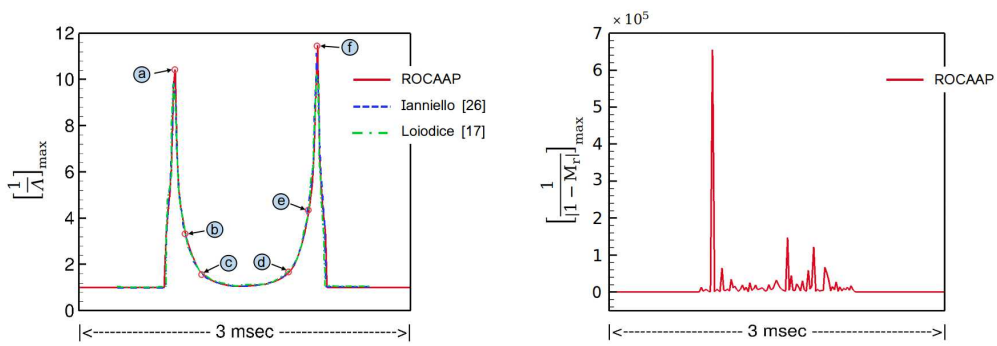

(a) $[1/\Lambda]_{max}$ (b) $[1/|1-M_r|]_{max}$

Figure 14: Time history of the integral kernel term.

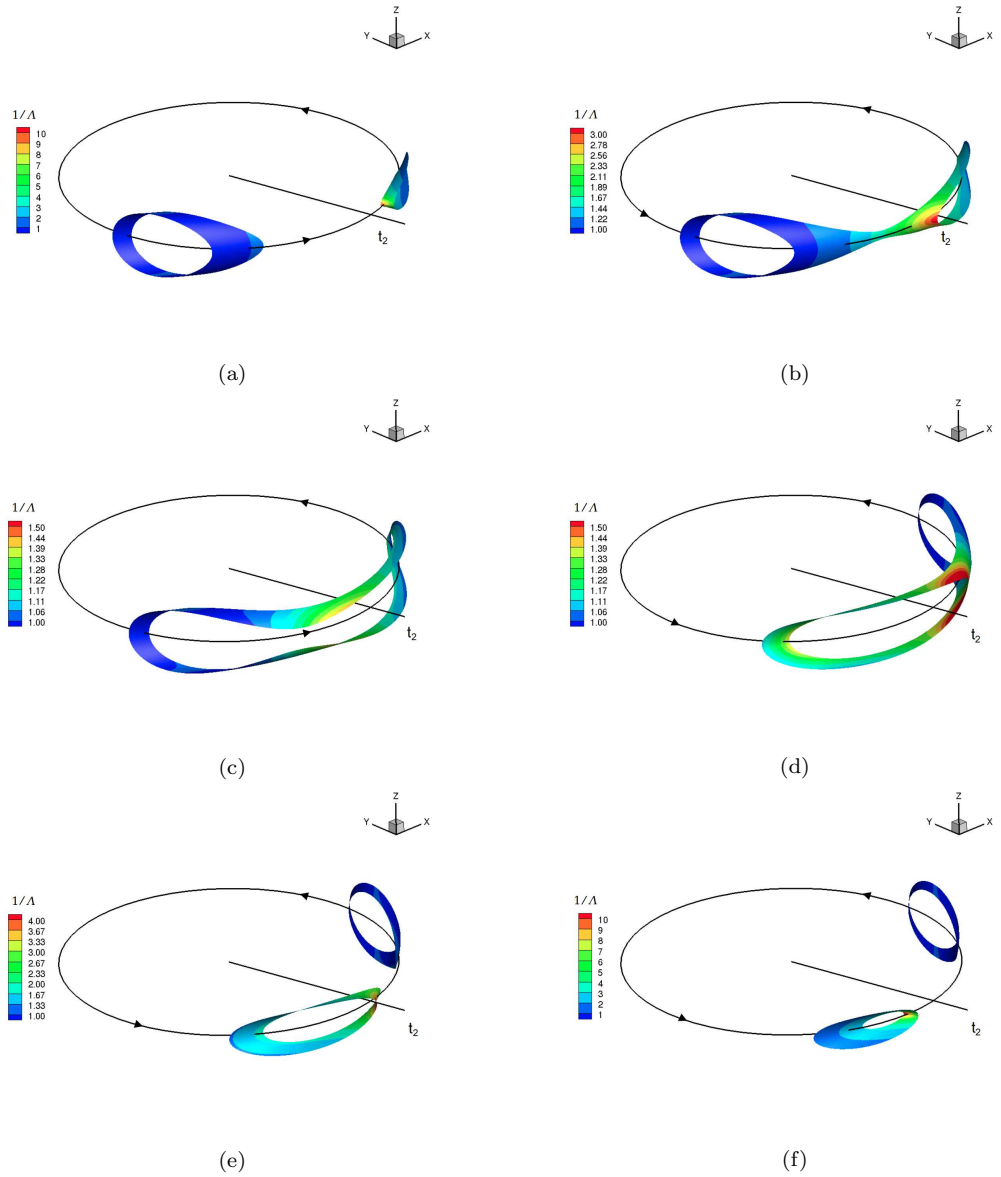

Figure 15: Σ surface of rotating cylindrical strip for six subsequent observer instants

4. Transonic rotor noise prediction

HSI noise is the primary source for helicopter rotor noise generation in transonic conditions. It is characterized by the quadrupole volume term in the FW-H equation. The intensity of HSI noise is closely related to the size and extension of the supersonic flow pocket, which appears at the blade tip region when the tip Mach number M_T is greater than the airfoil critical Mach number M_c. The supersonic pocket extends to the far-field beyond the sonic cylinder and connects the blade to the supersonic region when shock delocalization occurs. In such situations, the integration control surface should extend as far as possible from the blade tip and enclose all the quadrupole sources in the supersonic region. The Retarded-Time formulation of PS-FWH equation is well suitable for weak shock delocalization cases (see Ref [12]) but it becomes unusable for strong shock delocalization cases due to the acoustic integral singularity. As previously mentioned, the Emission-Surface formulation (Equation (7)) can avoid the effects of Doppler singularity by introducing a much less restrictive condition in the Doppler factor and give more accurate results for the cases with strong shock delocalization.

In Ref [28], an experimental set-up from the NASA Anechoic rotor hover test chamber was conducted to investigate the HSI phenomenon. The experiment refers to a UH-1H rotor in hover condition, where the blade tip Mach number is similar to the M_T values on the advancing side achieved in high-speed forward flight. The UH-1H rotor has two straight, untwisted blades with NACA0012 airfoil section. The blade span is 1.045 m and the airfoil chord is 0.07623 m. Five test conditions with blade tip Mach number ranging from 0.85 to 0.95 were employed in the experiment. The acoustic signals were measured in the rotor disc plane. This experiment is characterized by shock delocalization phenomena and can thus be considered a very suitable dataset for transonic rotor noise prediction. In the present work, three test conditions with $M_T = 0.85$, 0.88, and 0.95, which respectively corresponds to no delocalized shock, weak delocalized shock, and strong delocalized shock

phenomena (Figure 16), are used for the transonic rotor noise prediction. The noise prediction is carried out with the observer is located at 3.09 radii away from the rotor hub, laying in the rotor disc plane.

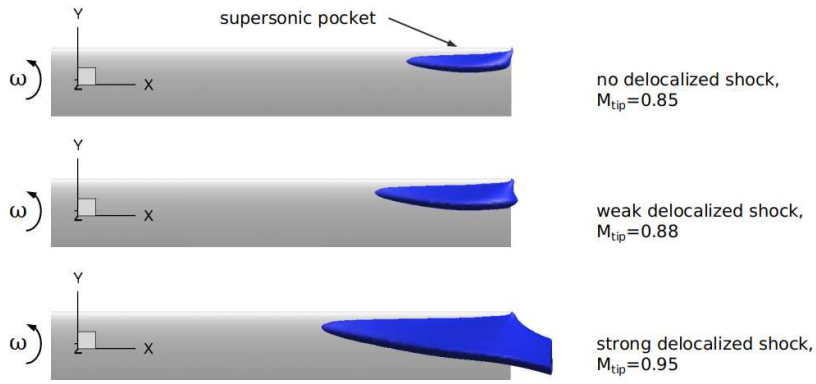

Figure 16: Shock delocalization phenomena

4.1. CFD grid sensitivity study

The acoustic prediction is much dependent on the aerodynamic results in any CFD/FW-H hybrid method. Hence, the grid sensitivity study is performed first to obtain the grid-independent solutions. Three different blade grid resolutions with $M_T = 0.85$, 0.88 and 0.95 are adopted for the grid sensitivity analysis. The details of the blade grids are summarized in Table 4. The results are compared in terms of Cp distributions along selected blade cross-sections. Figure 17 shows that sufficiently converged results are obtained with the medium grid, which is therefore used for the transonic noise prediction to guarantee precision and computational efficiency simultaneously.

4.2. Noise prediction of M_T = 0.85 and 0.88 cases

Two permeable control surfaces with different sizes are employed for assessing the sensitivity to the extension of the control surface. Regarding M_T

Table 4: Summary of the blade grids, employed for the UH-1H rotor simulations

Mesh	Blade elements				Volume cells (10^6)
	Upper	Lower	Span	Total	
Coarse	61	61	59	13942	1.7
Medium	89	89	59	19038	2.6
Fine	100	100	70	23680	3.9

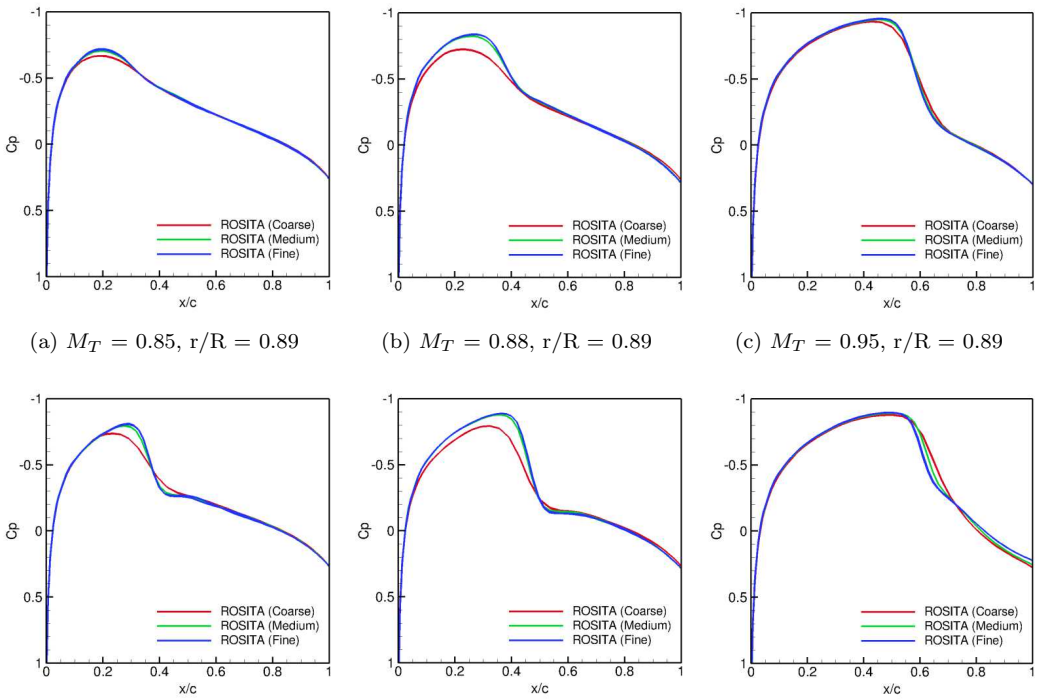

(a) $M_T = 0.85$, r/R = 0.89 (b) $M_T = 0.88$, r/R = 0.89 (c) $M_T = 0.95$, r/R = 0.89

(d) $M_T = 0.85$, r/R = 0.96 (e) $M_T = 0.88$, r/R = 0.96 (f) $M_T = 0.95$, r/R = 0.96

Figure 17: Cp distributions on two blade cross-sections for UH-1H rotor in hover mode

$= 0.85$ and 0.88 cases, the control surface may not be put far away from the rotor blade as the shock delocalization phenomenon is weak. Hence, the two control surfaces employed are $S1 = (1.5, 0.75)$ and $S2 = (1, 0.5)$. Figure 18 compares the noise predictions with two permeable control surfaces and experimental data [29]. These two control surfaces are seen to predict similar results with minor discrepancy. It is demonstrated that the far-field

noise predictions are not very sensitive to the choice of the numerical integration surface for both blade tip Mach numbers. Overall, the computed results have good agreement with the experimental noise measurements, although a slightly underpredicted negative peak pressure appears for the weak delocalized shock case ($M_T = 0.88$).

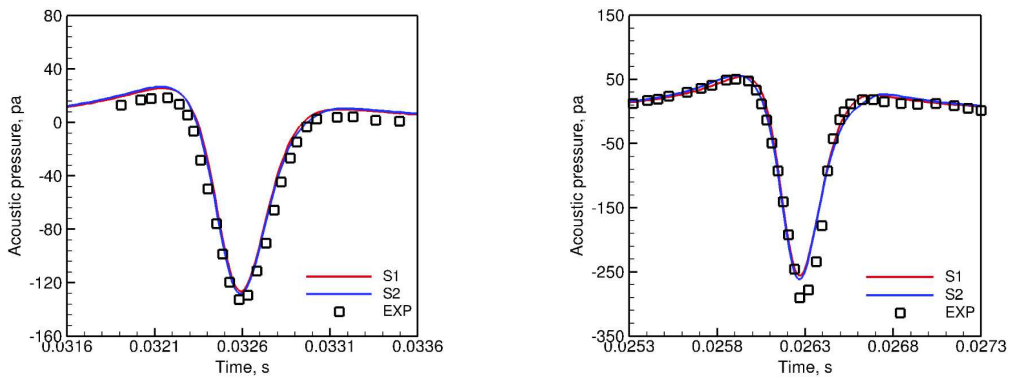

(a) $M_T = 0.85$ (b) $M_T = 0.88$

Figure 18: Predicted acoustic pressure comparison of different permeable control surfaces and experimental results.

4.3. Noise prediction of $M_T = 0.95$ case

When it comes to the significant shock delocalization case ($M_T = 0.95$), the integration control surface should be placed far away from the blade to enclose all the transonic flow regions. In order to analyze the sensitivity of the numerical solution provided by the MCES algorithm to the extension of control surface, six noise predictions with different sizes of control surface are carried out, as presented in Figure 19. The control surface $S = (0.5, 0)$ corresponds to the blade surface, the noise prediction is exactly provided by the IS-FWH formulation. Some undesirable impulses appeared on the predicted waveform as control surface moves away from the blade. With larger control surface used, these fluctuations are eliminated and the convergence result is

reached with control surface $S = (7.5, 1.25)$. These undesirable peaks may be due to the Λ singularity behavior.

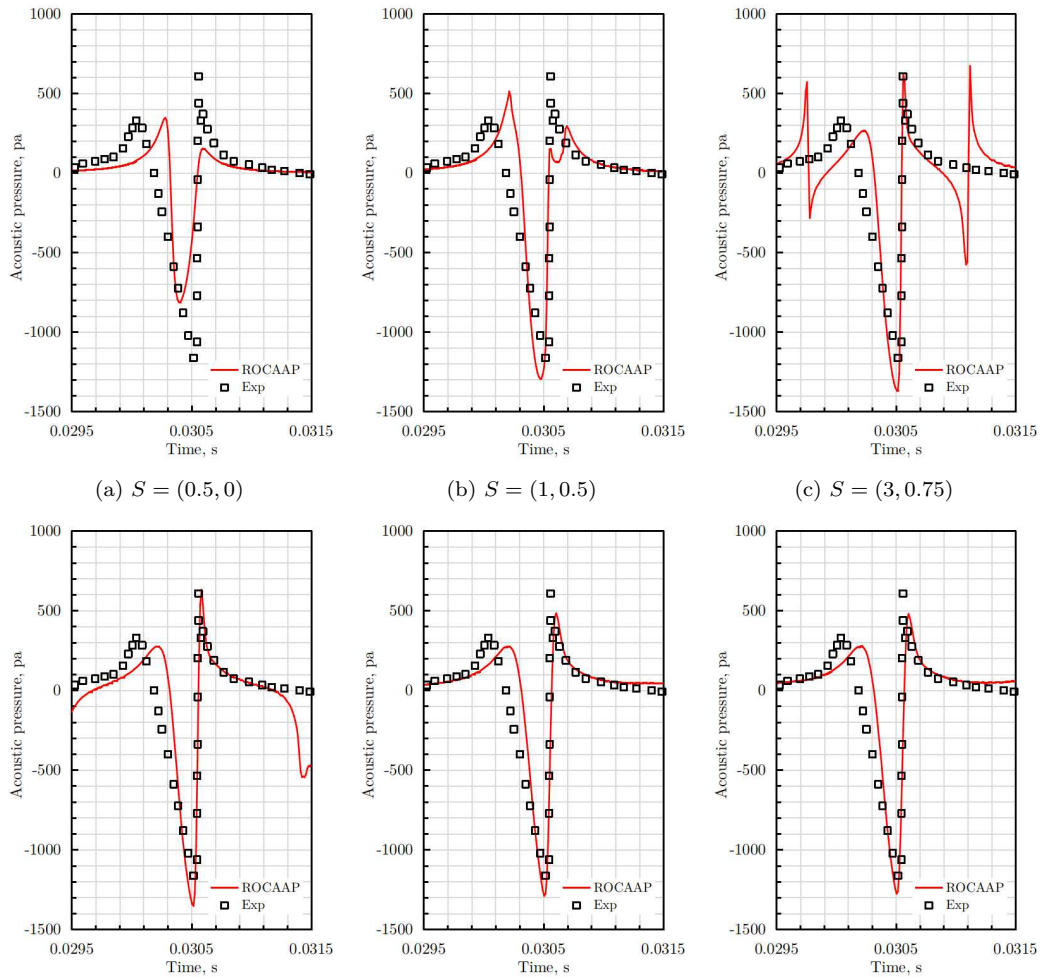

(a) $S = (0.5, 0)$ (b) $S = (1, 0.5)$ (c) $S = (3, 0.75)$

(d) $S = (5, 1)$ (e) $S = (7.5, 1.25)$ (f) $S = (9, 1.5)$

Figure 19: Convergence of the numerical prediction with respect ot the extension of control surface for strong shock delocalization case, $M_T = 0.95$.

In Figure 20, the MCES predictions are compared with the experimental data [29] and the solutions of K-Algorithm [27] and EPS method [17]. The MCES results agree overall with the measurements and the solutions calculated by the other two formulations. However, it is note that the negative

peak pressure and the slope in the first pressure drop exhibit a slight difference. These differences could be attributed to the CFD input data because the CFD grid was not refined in the direction of delocalized shock propagating. Nevertheless, the predicted noise signals have good agreement with the experiment in terms of the typical asymmetric waveform and the negative peak pressure. It is confirmed that the MCES PS-FWH method is capable of capturing both good peaks and shapes in the acoustic signal of the transonic rotor noise when the high shock delocalization occurs.

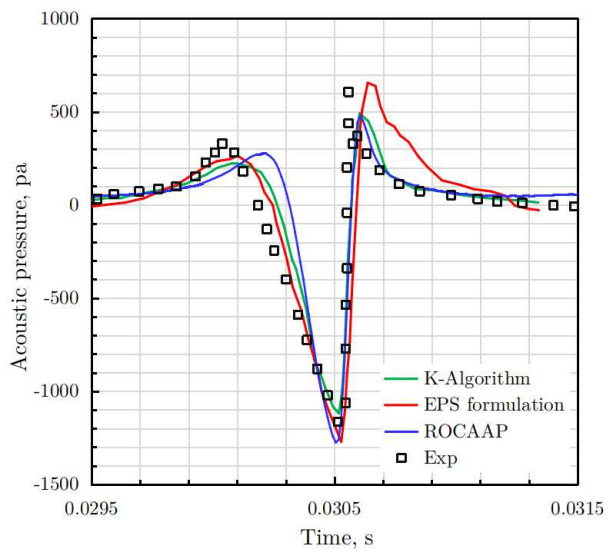

Figure 20: Noise prediction comparisons of different methods for $M_T = 0.95$

5. Conclusion

This work describes a CFD/PS-FWH hybrid method for modeling transonic rotor noise using the Chimera, multi-block, structured grid CFD solver ROSITA and the MCES based PS-FWH equation code ROCAAP. The prediction capabilities are demonstrated on several numerical simulations for preliminary validation. The hovering Caradonna-Tung rotor assessed the

CFD method with the pressure coefficient distributions at four various radial positions. The emission surface construction of non-realistic stationary spherical surface and rotational blade planform has allowed validating the Marching-Cube algorithm. The Λ singularity behavior of a rotating cylindrical strip was then modeled using the Marching-Cube approach. Finally, The proposed hybrid method was tested for the transonic rotor noise prediction with the well-known UH-1H rotor case at three opearating conditions ($M_T = 0.85$, 0.88, and 0.95), including weak and strong delocalization. The reasonable agreement achieved between the available experimental data and the predicted results confirm the effectiveness and robustness of the adopted computational approach.

In the future, research will concern the application of the proposed method to realistic high-speed forward flight helicopter rotors for the analysis of transonic noise phenomena.

Acknowledgement

We acknowledge the CINECA award under the ISCRA initiative, for the availability of high performance computing resources and support. The author Jinbin Fu, would like to thank the China Scholarship Council for financial support under the Grant (CSC, No.201706030145).

References

References

[1] K.S. Brentner, F. Farassat, An Analytical Comparison of the Acoustic Analogy and Kirchhoff Formulation for Moving Surfaces, AIAA J. 36 (1998) 1379-1385.

[2] B. Wang, Q. Zhao, G. Xu, L. Ye, J. Wang, Numerical analysis on noise of rotor with unconventional blade tips based on CFD/Kirchhoff method, Chinese J. Aeronaut. 26 (2013) 572-582.

[3] N.D. Polyzos, S. Vouros, I. Goulos, V. Pachidis, Multi-disciplinary optimization of variable rotor speed and active blade twist rotorcraft: Trade-off between noise and emissions, Aerosp. Sci. Technol. 107 (2020) 1-13.

[4] Y. Delorme, R. Stanly, S.H. Frankel, D. Greenblatt, Application of actuator line model for large eddy simulation of rotor noise control, Aerosp. Sci. Technol. 108 (2021) 1-12.

[5] S. Vouros, I. Goulos, V. Pachidis, Integrated methodology for the prediction of helicopter rotor noise at mission level, Aerosp. Sci. Technol. 89 (2019) 136-149.

[6] G. Romani, D. Casalino, Rotorcraft blade-vortex interaction noise prediction using the Lattice-Boltzmann method, Aerosp. Sci. Technol. 88 (2019) 147-157.

[7] L. Wang, G. Xu, Y. Shi, Development and validation of a hybrid method for predicting helicopter rotor impulsive noise, Proc. Inst. Mech. Eng. G: J. Aerosp. Eng.. 233 (2019) 1323-1339.

[8] J.E. Ffowcs Williams, D.L. Hawkings, Sound generation by turbulence and surfaces in arbitary motion, Philos. Trans. R. Soc. Lond. A, Math. Phys. Eng. Sci. 264 (1969) 321-342.

[9] K.S. Brentner, F. Farassat, Modeling aerodynamically generated sound of helicopter rotors, Prog. Aerosp. Sci. 39 (2003) 83-120.

[10] A.S. Lyrintizs, Review: The use of Kirchhoff's method in computational aeroacoustics, J. Fluids Eng. 116 (1994) 665-676.

[11] P.di Francescantonio, A new boundary integral formulation for the prediction of sound radiation, J. Sound Vib. 202 (1997) 491-509.

[12] A.S. Morgans, S.A. Karabasov, A.P. Dowling, T.P. Hynes, Transonic Helicopter Noise, AIAA J. 43 (2005) 1512-1524.

[13] S. Chen, Q. Zhao, Y. Ma, An adaptive integration surface for predicting transonic rotor noise in hovering and forward flights, Chinese J. Aeronaut. 32 (2019) 2047-2058.

[14] K.S. Brentner, A new algorithm for computing acoustic integrals, Proceedings of the IMACS 14th World Congress on Computational and Applied Mathematics. 2 (1994) 592-595.

[15] S. Ianniello, Algorithm to integrate the Ffowcs Williams-Hawkings equation on supersonic rotating domain, AIAA J. 37 (1999) 1040-1047.

[16] S. Ianniello, Aeroacoustic analysis of high tip-speed rotating blades, Aerosp. Sci. Technol. 5 (2001) 179-192.

[17] S. Loiodice, D. Drikakis, A. Kokkalis, Emission surfaces and noise prediction from rotating sources, J. Sound Vib. 429 (2018) 245-264.

[18] L. Vendemini, L. Vigevano, An emission surface approach for noise propagation from high speed sources, in: 43rd European Rotorcraft Forum, Milano, Italy, 2017.

[19] F. Farassat, K.S. Brentner, Supersonic quadrupole noise theory for high-speed helicopter rotors, J. Sound Vib. 218 (1998) 481-500.

[20] S. Ianniello, The K-algorithm and the modeling of the emission surface from supersonically rotating bodies, J. Comput. Phys. 408 (2020) 1-30.

[21] S. Loiodice, D. Drikakis, A. Kokkalis, An efficient algorithm for the retarded time equation for noise from rotating sources, J. Sound Vib. 412 (2018) 336-348.

[22] M. Biava, L. Vigevano, Simulation of a complete helicopter: A CFD approach to the study of interference effects, Aerosp. Sci. Technol. 19 (2012) 37-49.

[23] C. Montari, R. Scateni, R. Scopigno, A modified look-up table for implicit disambiguation of marching cubes, Vis Comput. 10 (1994) 353-355.

[24] S. Loiodice, Modelling noise from rotating sources in subsonic and supersonic regimes, Ph.D thesis, Cranfield University, 2008.

[25] G. Chesshire, W.D. Henshaw, Composite overlapping meshes for the solution of partial differential equations, J. Comput. Phys. 90 (1990) 1-64.

[26] F.X. Caradonna, C. Tung, Experimental and analytical studies of a model helicopter rotor in hover, NASA TM-81232, 1981.

[27] S. Ianniello, New perspectives in the use of the Ffowcs Williams-Hawkings equation for aeroacoustic analysis of rotating blades, J. Fluid Mech.. 570 (2007) 79-127.

[28] D.A. Boxwell, Y.H. Yu, F.H. Schmitz, Hovering impulsive noise: some measured and calculated results, Vertica. 3 (1979) 35-45.

[29] T.W. Purcell, CFD and transonic helicopter sound, in: 14th European Rotorcraft Forum, Milano, Italy, 1988.